This article has been accepted for inclusion in a future issue of this journal. Content is final as presented, with the exception of pagination.

An SEM-Based Nanomanipulation System for Multiphysical Characterization of Single InGaN/GaN Nanowires

Juntian Qu, *Member, IEEE*, Renjie Wang, Peng Pan, *Member, IEEE*, Linghao Du, Zetian Mi, *Fellow, IEEE*, Yu Sun, *Fellow, IEEE*, and Xinyu Liu, *Member, IEEE*

***Abstract*— Nanomaterials possess superior mechanical, electrical, and optical properties suitable for device applications in different fields such as nanoelectronics, photonics, and sensors. Characterizing the multiphysical properties of single nanomaterials and nanostructures provides experimental guidelines for synthesis and device applications of functional nanomaterials. Nanomanipulation techniques under scanning electron microscopy (SEM) have enabled the testing of mechanical and electrical properties of various nanomaterials. However, the introduction of micro-photoluminescence (μ-PL) measurement into an SEM setup for *in-situ* single nanomaterial characterization is still experimentally challenging; in particular, the seamless integration of the mechanical, electrical, and μ-PL testing techniques inside an SEM for multi-field-coupled characterization of single nanostructures is still unexplored. In this work, we report the first SEM-based nanomanipulation system for multiphysical characterization of single nanomaterials. A custom-made, optical-microfiber-based μ-PL setup is integrated onto a nanomanipulation system with four nanomanipulators inside an SEM. The system is also equipped with a conductive nanoprobe and a conductive atomic force microscopy (AFM) probe for electrical nanoprobing and electroluminescence (EL) measurement of single nanomaterials with contact force feedback. Using the system, field-coupled characterization (i.e., optomechanical, optoelectronic, electromechanical, and mechano-optoelectronic testing) of single InGaN/GaN nanowires (NWs) are conducted; and, for the first time, the effect of mechanical compression applied to individual InGaN/GaN NWs on its optoelectronic property is revealed.**

***Note to Practitioners*—With the rapid advances of nanophotonics and nanoelectronics, the optical and optoelectronic characterization of semiconductive nanomaterials becomes widely used for guiding the material synthesis and improving the nanodevice performance. However, few studies on optical-relevant characterization were carried out in SEM, mainly due to the limited space of an SEM chamber, making it challenging to integrate optical components for effective optical excitation and luminescence measurement. To address this issue, space-saving optical microfibers were integrated into the SEM chamber for *in-situ* optoelectronic characterization of semiconductor NWs, along with the seamless integration of mechanical and electrical nanoprobing tools for electromechanical characterization. The developed nanomanipulation system will greatly facilitate the multiphysical testing of semiconductor nanomaterials, and thus expedite their synthesis optimization processes and broaden their optoelectronic device applications.**

***Index Terms*— Multiphysical characterization, nanomanipulation, scanning electron microscopy, semiconductive nanomaterials, InGaN/GaN nanowires.**

Manuscript received October 29, 2021; accepted December 28, 2021. This article was recommended for publication by Associate Editor H. Choi and Editor D. O. Popa upon evaluation of the reviewers' comments. This work was supported in part by the Natural Sciences and Engineering Research Council of Canada under Grant RGPIN-2017-06374 and Grant RGPAS-2017-507980, in part by the University of Toronto, and in part by the National Natural Science Foundation of China under Grant 52103283. *(Corresponding author: Xinyu Liu.)*

Juntian Qu is with the Department of Mechanical and Industrial Engineering, University of Toronto, Toronto, ON M5S 3G8, Canada, also with the Department of Mechanical Engineering, McGill University, Montreal, QC H3A 0C3, Canada, also with the Department of Mechanical Engineering, Tsinghua University, Beijing 100084, China, and also with the Tsinghua Shenzhen International Graduate School, Shenzhen 518055, China.

Renjie Wang is with the Department of Electrical and Computer Engineering, McGill University, Montreal, QC H3A 0C3, Canada.

Peng Pan and Xinyu Liu are with the Department of Mechanical and Industrial Engineering, University of Toronto, Toronto, ON M5S 3G8, Canada, and also with the Department of Mechanical Engineering, McGill University, Montreal, QC H3A 0C3, Canada (e-mail: xyliu@mie.utoronto.ca).

Linghao Du and Yu Sun are with the Department of Mechanical and Industrial Engineering, University of Toronto, Toronto, ON M5S 3G8, Canada.

Zetian Mi is with the Department of Electrical Engineering and Computer Science, University of Michigan, Ann Arbor, MI 48109 USA, and also with the Department of Electrical and Computer Engineering, McGill University, Montreal, QC H3A 0C3, Canada.

Color versions of one or more figures in this article are available at https://doi.org/10.1109/TASE.2022.3146486.

Digital Object Identifier 10.1109/TASE.2022.3146486

I. Introduction

THE last two decades have witnessed signifiant advances in the field of nanomaterials. Due to their unique nanoscale morphologies and superior physical/chemical properties, nanomaterials have been widely used for a variety of applications such as next-generation electronics [1], nanocomposite synthesis [2], sustainable energy [3], biosensing [4] and photonics [5]. The mechanical, electrical, optical, and field-coupled (e.g., electromechanical, optoelectronic, and mechno-optoelectronic) properties of these nanomaterials play critical roles in their practical applications; thus, the experimental characterization of these properties is of major concern from perspectives of both nanomaterial synthesis and device applications.

Among various experimental techniques employed for nanomaterial characterization, scanning electron microscopy (SEM)-based nanomanipulation has been applied to testing the mechanical, electrical, and electro-mechanical properties of different types of nanomaterials and nanostructures [6]–[17].

1545-5955 © 2022 IEEE. Personal use is permitted, but republication/redistribution requires IEEE permission.
See https://www.ieee.org/publications/rights/index.html for more information.

Authorized licensed use limited to: The University of Toronto. Downloaded on March 24,2022 at 15:58:40 UTC from IEEE Xplore. Restrictions apply.

This article has been accepted for inclusion in a future issue of this journal. Content is final as presented, with the exception of pagination.

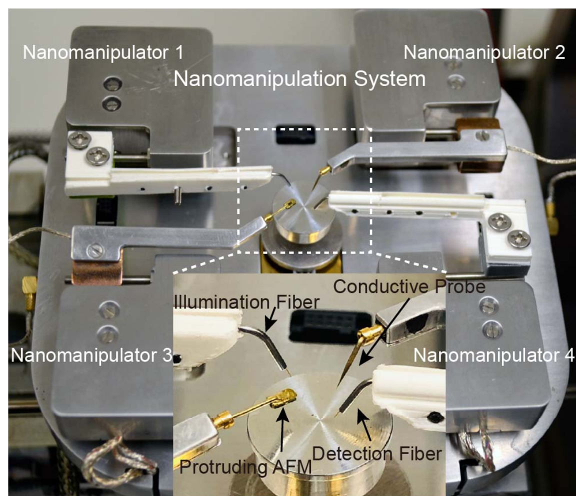

Fig. 1. Photographs of the SEM-based nanomanipulation system. The inset shows the zoomed-in view of one protruding AFM probe, one conductive nanoprobe, and two optical microfibers mounted on the four nanomanipulators.

Compared to the atomic force microscopy (AFM)-based nanomanipulation techniques [18]–[24], SEM provides direct visual feedback with a high frame rate and high resolution; besides, the substantially larger field of view (several millimeters; AFM: maximum about 150 μm × 150 μm) and real-time nanometer-level imaging resolution of SEM enable simultaneous nanomaterial imaging and manipulation [6], [25].

With the rapid advances of nanophotonics and nanoelectronics, the optical and optoelectronic characterization of semiconductive nanomaterials becomes widely used for guiding the material synthesis and improving the nanodevice performance. For optical characterization, only a few studies on cathodoluminescence (CL) characterization of nanomaterials [26]–[29] were carried out in SEM. For optoelectronic characterization, the SEM was only utilized for focused ion beam (FIB)-assisted metal contact deposition [30]; the major characterization processes were still performed in the ambient environment. The lack of SEM-based optical characterization setup is mainly due to the limited space of an SEM chamber, making it challenging to integrate optical components for effective optical excitation and luminescence measurement [31].

To perform optical characterization of single nanomaterials (i.e., micro-photoluminescence or μ-PL) inside an SEM, efficient light collection and luminescence detection are necessary. A sizeable paraboloidal mirror was employed in an SEM [31] for light collection in CL testing; however, due to the limited space of the SEM chamber, the mirror blocked most other detectors and did not allow electrical nanoprobe integration, thus hindering the simultaneous supply and measurement of electrical and optical signals on the nanomaterial. To address this issue, space-saving optical microfibers [29] were integrated into an SEM chamber for *in-situ* optoelectronic characterization of semiconductor nanowires (NWs). However, the experimental setup does not possess force sensing capability to quantify contact forces applied to a nanostructure for studying the mechanical effect on the material's optical, electrical and optoelectronic properties. Based on above discussions, it is highly desired to develop an SEM-based system capable of characterizing the mechanical, electrical, optical, and field-coupled properties of single nanomaterials.

In this paper, we report the first SEM-based nanomanipulation system mechanical, electrical, and optical measurement capabilities for multiphysical characterization of single semiconductor NWs. Through seamless integration of a custom-made, optical-microfiber-based μ-PL setup with mechanical and electrical nanoprobing tools inside an SEM, we develop experimental strategies for performing *in-situ* characterization of field-coupled properties on single InGaN/GaN NWs. We demonstrate optomechanial, optoelectronic, electromechanical, and mechano-optoelectronic characterization of InGaN/GaN NWs, and investigate, for the first time, the effect of mechanical compression on the electroluminescence (EL) property of single InGaN/GaN NWs. The developed nanomanipulation system will greatly facilitate the multiphysical testing of semiconductor nanomaterials, thus expedite their synthesis optimization processes and broaden their optoelectronic device applications.

This paper is an extended version of a previous conference paper that only reports the mechano-optoelectronic testing results [32]. In this extended journal version, we performed more calibration experiments of the optical (μ-PL) testing module, and carried out three additional field-coupled characterization experiments (i.e., optomechanical, optoelectronic and electromechanical testing) on single InGaN/GaN NWs to fully demonstrate the system's unique nanomaterial testing capabilities. More technical details, experimental results, and discussions are included.

II. Nanomanipulation System Development

A. System Overview

Fig. 1 shows the photograph of the nanomainpulation system setup. Housed inside an SEM (SU3500, Hitachi; not shown in Fig. 1), the setup is based on a piezoelectric nanomanipulator with four closed-loop controlled nanopositioners (LF-2000, Toronto Nanoinstrumentation Inc.). One Pt-coating conductive tungsten nanoprobe (ST-20-0.5, GGB Industries), one Pt-coating conductive AFM cantilever probe with a protruding tip (ATEC-FM, NanoAndMore Corp.), and two optical microfibers (Accu-Glass Products Inc.) are mounted on the four nanopositioners, with the nanoprobe and AFM probe arranged along one diagonal direction and the two optical microfibers along the other diagonal direction. The system also contains necessary components for operation in three single-field testing modes: (i) the electrical testing mode, (ii) the optical testing mode, and (iii) the mechanical testing mode. With the seamless integration of all the testing components and the development of corresponding techniques, the system is capable of executing single-field and field-coupled characterization tasks.

The Pt-coated tungsten nanoprobe and the AFM cantilever probe can be used for *in-situ* electrical probing of nanomaterials such as the as-grown single NWs on its growth substrate. Owing to its protruding tip visible from the SEM

Authorized licensed use limited to: The University of Toronto. Downloaded on March 24,2022 at 15:58:40 UTC from IEEE Xplore. Restrictions apply.

This article has been accepted for inclusion in a future issue of this journal. Content is final as presented, with the exception of pagination.

top view, the AFM cantilever probe can be guided by the SEM vision to contact the top surface of a single NW, without requiring the SEM sample stage to be tilted for observing the side view of the probe and the NW sample. For applying an electrical voltage/current to a NW sample, our system employs two-point electrical nanoprobing rather than adopting the conventional electron-beam lithography (EBL)-patterned electrode contacts, which avoids chemical treatment of the NW sample during EBL [33], [34]. Through SEM visual guidance, the two optical microfibers can be precisely positioned to the proximity of a single NW for optical excitation and luminescence measurement (i.e., μ-PL measurement). Besides, the protruding AFM probe can also serve as a high-resolution force sensor for contact force measurement during nanoprobing, which, in combination with the SEM-based motion tracking, enables mechanical characterization and stimulation (by applying strain/stress) of single NWs.

The major merit of this multiphysical characterization system is the flexibility of combining different types of end-effectors for different tasks. By combining both the luminescence detection microfiber and the two conductive probes, we can perform optoelectronic (i.e., EL) characterization of a single NW, where the injection current can be applied to the NW using the two conductive probes and the resulting optical emission can be simultaneously measured by the optical microfiber. Moreover, this system can also be extended to triple-field-coupled (mechano-optoelectronic) characterization. For the triple-field-coupled characterization, a single semiconductor NW is compressed by the AFM probe from the top at a desired contact force level, and the effect of the induced NW stress/strain on its EL property is quantified by the two conductive probes and the luminescence detection microfiber. In this operation, the conductive AFM probe serves as both the electrical nanoprobe and the force-sensing end-effector. In the following sections, we will introduce the optical, mechanical and electrical characterization modules of the nanomanipulation system.

B. Optical Testing Mode

1) Optical Setup Design: In the optical testing mode, the system employs the space-saving optical microfibers for laser excitation and luminescence measurement on the NW. Fig. 2(a) shows the schematic diagram of the optical characterization setup. A 405 nm collimated diode laser (LRD-0405-PFR-00500-05, Laserglow Technologies) was chosen as the optical excitation source, and the laser beam was guided into the SEM chamber through two multimode optical microfibers: one 100 μm UV/VIS bare polished fiber (112550, Accu-Glass Products Inc.) inside the SEM vacuum chamber (the vacuum side) and another 100 μm UV/VIS PMMA-encapsulated fiber (112552, Accu-Glass Products Inc.) outside the SEM chamber (the air side). A custom-made vacuum feedthrough was mounted on a port of the SEM chamber for connecting the two microfibers and coupling the laser beam from outside to inside of the chamber. To protect the fragile thin bare microfiber in the SEM chamber, a soft tube of 150 μm inner diameter (ID) was utilized to sheathe the vacuum-side bare

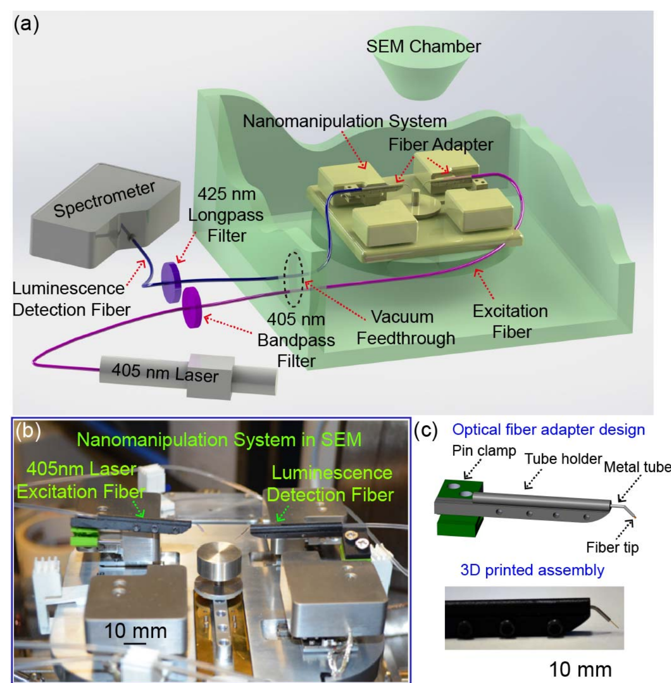

Fig. 2. SEM-based optical characterization module. (a) Schematic and (b) photograph of the optical characterization module with two integrated optical fibers. (c) Schematic and photograph of the optical fiber adapter.

microfiber. Finally, to complete the excitation loop setup, a 405 nm bandpass filter (OD4, Edmund Optics) was set in the path of air-side microfiber for selectively passing the 405 nm excitation signal.

To detect the optical emission from a NW, two optical microfibers of the same type (wavelength range: 200-800 nm) were selected for mounting at both the air- and vacuum-sides of the SEM. The selection of the visible wavelength range meets the requirement of PL and EL measurements of the InGaN/GaN NWs. Another custom-made vacuum feedthrough was mounted on the same SEM chamber port for connecting the microfibers and pass through the collected sample emission signal to outside of the SEM chamber. The end of the air-side luminescence detection microfiber was connected to a high-precision spectrometer (Ocean Optics, QE Pro-FL) with a back-thinned, thermoelectrically (TE)-cooled CCD detector for luminescence measurement. To isolate the luminescence signal from the 405 nm excitation signal, a 425 nm longpass filter (OD4, Edmund Optics) was placed in the air-side detection path for filtering out any 405 nm signal.

A technical challenge for integration of the optical characterization setup was how to mount the two thin flexible bare microfiber tips onto the nanopositioners and achieve fixed light excitation and detection angles. As shown in Fig. 2(c), we designed an adapter to stably mount a bare microfiber onto the nanopositioner. The flexible optical microfiber tip was firstly inserted into a metal tube with a 45° bending angle, and the metal tube was then inserted into a protection tube with an inner diameter of 150 μm. A 3D-printed tube holder was fabricated to immobilize the protection tube, and a custom-made pin clamp was integrated at the end of the tube

Authorized licensed use limited to: The University of Toronto. Downloaded on March 24,2022 at 15:58:40 UTC from IEEE Xplore. Restrictions apply.

This article has been accepted for inclusion in a future issue of this journal. Content is final as presented, with the exception of pagination.

holder for firmly clamping it onto the output pin shaft of the nanopositioner. This adapter design provides stable mounting of the two microfibers onto the two nanopositioners, and also allows the microfiber position and bending angle to be readily adjusted by changing the clamp position on the metal pin of the nanopositioner and the bending angle of the metal tube, respectively. Fig. 2(b) shows the laser excitation microfiber and the luminescence detection microfiber stably mounted on the nanomanipulator.

2) Optical Module Calibration: To quantify the output illumination power at the excitation microfiber tip, we calibrated the entire excitation loop and obtained the data of total output power at the microfiber tip vs. driving current of the laser source. A digital optical power meter (PM100D, Thorlabs) with a 200-1000 nm photodiode power sensor (S120VC, Thorlabs) was utilized for this task, with the sensing probe of the meter covering the whole excitation fiber tip to minimize the energy loss during measurement. The calibration curve is shown in Fig. 3(a). One can observe a dead zone in the driving current range of less than 0.024 A, beyond which the laser power and driving current have a nonlinear correlation until 0.03 A [inset of Fig. 3(a)]. For any driving current over 0.03 A, the corresponding output laser power at the microfiber tip is linearly proportional to the driving current of the laser source. The maximum output laser power from the microfiber tip was 43.7 mW at the driving current of 0.37 A [Fig. 3(a)].

In the luminescence detection loop, there is transmission loss existing in the optical coupling between air-side/vacuum-side optical fibers and the vacuum feedthrough. To derive the original luminescence intensity at the detection fiber tip inside the SEM chamber, we performed a calibration of the detection loop transmission rate using a broad range tungsten halogen source (HL-2000, Ocean Optics) and the QE-Pro spectrometer, where light was coupled into the detection optical fiber (inside SEM chamber) and the transmitted remaining light was detected at the other end outside chamber. The transmission rate in the wavelength range of 400-900 nm is plotted in Fig. 3(b). One can see the rate is over 50% in the wavelength range of 450-900 nm. Considering light coupling among multiple components and the additional loss caused by microfiber bending, the measured transmission rate of the luminescence detection loop is acceptable.

As environmental temperature is a crucial factor that affects the optoelectronic properties of semiconductor nanomaterials, we also calibrated the environmental temperature change induced by the e-beam and laser illumination in the enclosed SEM vacuum chamber (vacuum level: $\sim 3.33 \times 10^{-4}$ Pa). A digital temperature sensor (TMP 102, Sparkfun Electronics) was mounted onto the sample holder of the nanomanipulation system to measure the environmental temperature rise after two minutes of e-beam and laser illumination, which was the maximum illumination period in our experiments. As shown in the Fig. 3(c), it was verified that the e-beam irradiation has no obvious impact on the environmental temperature for 2 min continuous irradiation. Fig. 3(d) shows the environmental temperature rise curve during 2 min continuous laser illumination at the power of 21.5 mW (which will be used for InGaN/GaN NW testing). Due to the slow thermal convection rate in the

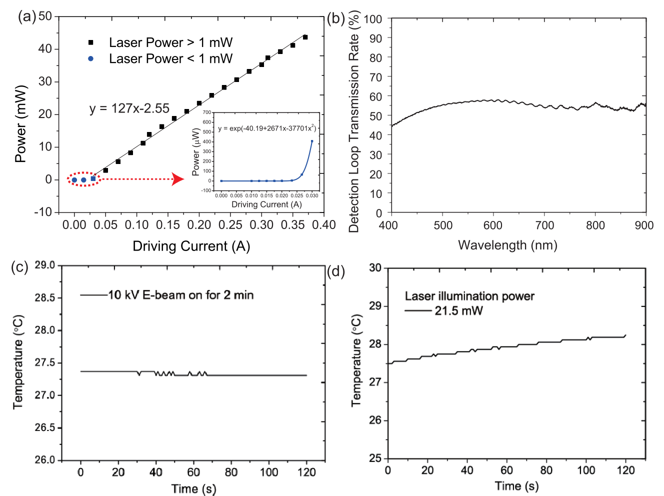

Fig. 3. Calibration data of the optical characterization module. (a) Illumination power vs. driving current of the laser source. (b) Optical transmission rate of the luminescence detection loop vs. wavelength. (c) Environmental temperature vs. the e-beam irradiation time. (d) Environmental temperature vs. laser illumination time.

enclosed vacuum chamber, we observed a ~0.5°C temperature rise after 2 min continuous laser illumination. To mitigate the environmental temperature effect on the optoelectronic property of the sample, the luminescence measurement was completed within 1 min, during which the corresponding temperature rise was less than 0.3°C [Fig. 3(d)].

C. Mechanical Testing Mode

In the mechanical testing mode, the system employs the protruding AFM probe tip to contact the top surface of a single NW at different desired contact force levels for examining the mechanical impact on the optical and optoelectronic properties of the NW. Due to its protruding shape (right of Fig. 4), the AFM probe tip is visible from the SEM top view, making it easy to visualize the contact between the protruding tip and the NW top surface (left of Fig. 6). Thus, we can readily establish stable contact between the AFM probe tip and the NW top surface. In this type of manipulation, the protruding AFM tip serves both a force sensor for contact force measurement and an electrical probe for optoelectronic characterization of the NW.

The protruding AFM probe was mounted onto the nanopositioner with three translational degrees of freedom (DOF) with a positioning resolution of 0.1 nm along each axis. To quantify the force applied to a NW by the AFM tip, the AFM cantilever beam deflection needs to be measured. However, from the SEM top view, the cantilever beam deflection cannot be visualized. In order to visually measure the cantilever beam deflection, we mounted the NW sample onto a 90° tilting holder. For better visualizing the probe tip-NW contact, the SEM stage was tilted at 10°. Equivalently, the NWs sample was tilted at 80° relative to the original horizontal plane [see SEM photographs in Fig. 5(b)]. With the NW-tilting setup, an experimental protocol was developed to calculate the AFM contact force on the top surface of a single NW,

Authorized licensed use limited to: The University of Toronto. Downloaded on March 24,2022 at 15:58:40 UTC from IEEE Xplore. Restrictions apply.

This article has been accepted for inclusion in a future issue of this journal. Content is final as presented, with the exception of pagination.

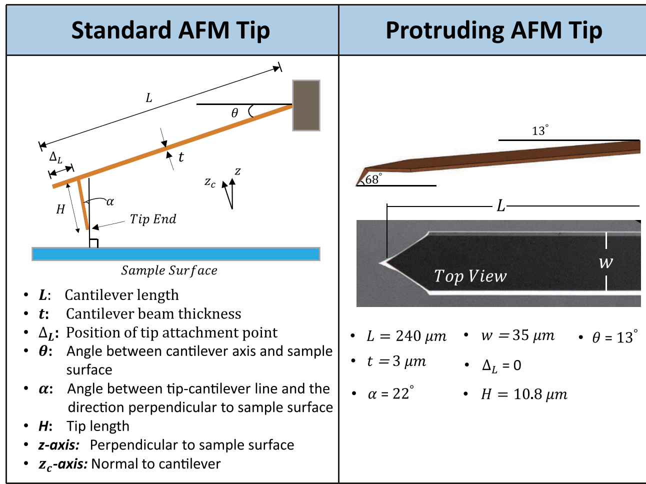

Fig. 4. Two types of AFM cantilever tip geometry: the standard AFM tip and the protruding AFM tip.

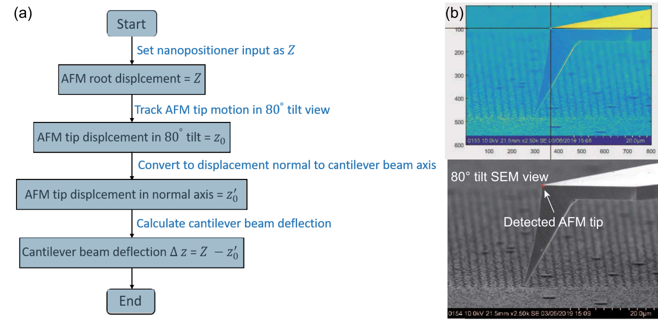

Fig. 5. Vision-based tracking of cantilever beam deflection. (a) Flow chart. (b) Vision tracking of AFM tip motion at an 80° tilting angle.

Stiffness Correction	Torque Correction
• F_z: Force applied to single NW • Δ_z: Cantilever beam deflection • k_c: Intrinsic spring constant, fundamental stiffness perpendicular to the long axis of the cantilever • k_z: Effective cantilever stiffness perpendicular to the horizontal sample surface. $k_z = \frac{k_c}{\cos^2\theta}$ L, θ, Δ_z, z_c, z, k_c, k_z, NW, F_z, Sample Substrate $k_z = \frac{k_c}{\cos^2\theta} = \frac{2.4178}{\cos^2 13^\circ} = 2.546$ N/m	• T_z: Torque correction perpendicular to sample • k_c: Intrinsic stiffness of cantilever $k_c = \frac{Ewt^3}{4L^3}$ • $k_{z\theta}$: Spring constant relating to longitudinal torque $k_{z\theta} = \frac{Ewt^3}{6L^3}$ $T_z = (1 - H\frac{k_c}{k_{z\theta}}\frac{\sin\alpha}{\cos\theta})^{-1}$ $\frac{k_c}{k_{z\theta}} = \frac{3}{2L}$ $\frac{\sin\alpha}{\cos\theta} = 0.3844$ $T_z = 1.027$

Fig. 6. Calculations for cantilever stiffness correction (left) and longitudinal torque correction (right).

which includes three steps: (i) vision-based measurement of the cantilever beam deflection, (ii) AFM cantilever stiffness correction, and (iii) longitudinal torque correction.

1) Vision-Based Tracking of Cantilever Beam Deflection: During nanoprobing of a NW, the AFM cantilever beam deflection can be calculated as the displacement difference between the root of cantilever beam and the AFM tip. As the cantilever root was firmly connected with the nanopositioner, its displacement was read as the nanopositioner displacement, Z. In the 80°-tilting SEM view, we tracked the AFM tip displacement through a simple corner detection algorithm [Fig. 5(b)] and obtained the AFM tip displacement, z_0. Denote the tip displacement normal to the cantilever beam axis as z_0', and we calculated $z_0' = z_0/\sin 80°$. Then the cantilever beam deflection Δz can be calculated as $\Delta z = Z - z_0'$. The whole flow of measuring the AFM cantilever beam deflection is shown in Fig. 5(a).

2) AFM Cantilever Stiffness Correction: After obtaining the AFM cantilever beam deflection, it is necessary to calibrate the cantilever stiffness so that the contact force could be accurately calculated. During NW probing, the AFM cantilever was inclined at 13° (left of Fig 6) to allow its tip to access the sample top surface without interference between the cantilever holder (at its root) and the sample substrate. Since the cantilever tilting angle affects the effective stiffness of the AFM cantilever, the cantilever stiffness in the tilting setup should be corrected based on the tilting angle [35].

The relationship between the cantilever effective stiffness and the tilting angle θ has been experimentally verified in a previous study using a microfabricated AFM cantilever [35]. The effective stiffness was determined to be $k_z = k_c/\cos^2\theta$, where k_c is the intrinsic stiffness perpendicular to the long axis of the cantilever. Detailed schematic illustration of the tilting setup and effective stiffness correction is shown in Fig. 6 (left). To calibrate the intrinsic stiffness k_c, the thermal tune method [36], based on thermal noise measurement, provides an automated and quick determination of cantilever spring constant. The cantilever deflection sensitivity was first calibrated as 41.67 nm/V using a commercial AFM (Bioscope Resolve, Bruker). The power spectral density (PSD) data were fitted using the Lorentzian (Air) model to derive the intrinsic stiffness of the AFM cantilever to be 2.4178 N/m. The effective stiffness of the protruding AFM cantilever in the 13° tilting setup was finally calculated to be 2.546 N/m.

3) Torque Correction: According to a general theoretical model [37], we can derive the applied AFM tip force (F_z in the left of Fig. 6) normal to the sample surface to be $F_z = k_z \Delta z T_z$, where k_z is the effective cantilever stiffness normal to the sample surface, Δz the obtained cantilever deflection, T_z the induced AFM tip torque correction factor in the presence of cantilever tilt [37]. Detailed derivation and calculation of T_z can be found in Fig. 6 (right). For our 13°-tilted protruding AFM tip, the torque correction factor T_z was calculated to be 1.027.

D. Electrical Testing Mode

In the electrical testing mode, the system functions as a two-point electrical nanoprobing setup. The Pt-coated tungsten nanoprobe and the conductive protruding AFM cantilever probe can be used for *in-situ* electrical nanoprobing. In a

Authorized licensed use limited to: The University of Toronto. Downloaded on March 24,2022 at 15:58:40 UTC from IEEE Xplore. Restrictions apply.

This article has been accepted for inclusion in a future issue of this journal. Content is final as presented, with the exception of pagination.

previous work [38], we have performed a systematic investigation of the experimental strategies for reducing the contact resistance between the conductive nanoprobe and the sample for *in-situ* nanomaterial probing without requiring metal electrode patterning. In this research, we followed the same two-point nanoprobing protocol reported in [38] to reduce the e-beam-induced contaminant deposition and thus minimize the probe-sample contact resistance.

III. Field-Coupled Characterization Experiments

To demonstrate the field-coupled nanomaterial characterization using the nanomanipulation system, we conducted four types of field-coupled characterization experiments including optomechanical, optoelectronic, electrochemical, and mechano-optoelectronic testing. Single InGaN/GaN NWs were chosen for the demonstrations because of its intrinsic piezoelectric property, excellent light emission characteristics, and crucial role in optoelectronic applications such as high-efficiency white light-emitting diodes (LEDs) [39] and deep-UV laser sources [40].

A. InGaN/GaN NW Synthesis

We fabricated single InGaN/GaN quantum-dot (QD) NWs with diameters of 200–600 nm on a Si substrate by selective area epitaxy (SAE) using a radio frequency plasma-assisted molecular beam epitaxy system (PA-MBE; GENxplor, Veeco). The epitaxy took place on an arsenic doped n-type Si substrate with a 10 nm Ti layer as the growth mask [41], [42]. Opening sizes in the range of 200–600 nm were created on the Ti mask using EBL and reactive ion etching, and the opening size precisely controlled the NW diameter.

As schematically shown in Fig. 7(a), each NW consists of a ∼450 nm-long n-type Si-doped GaN segment, six vertically aligned InGaN/GaN (4 nm/4 nm) quantum dots and a ∼150 nm-long p-type Mg-doped GaN segment. The average height of the NWs was ∼650 nm. Fig. 7(b) shows the SEM photograph (45°-tilting view) of a single NW grown on a Si substrate. The NW exhibits hexagonal morphology and possesses Ga-polarity based on the terminating facets.

B. Optomechanical Characterization

PL characterization is a contactless and nondestructive method for probing the electronic structure of semiconductor nanomaterials. With the μ-PL setup integrated into the SEM, we were able to study the optomechanical testing of single InGaN/GaN NWs and examine the PL spectrum change of the NW under different contact/compression force levels applied by the protruding AFM cantilever tip. The diameter of the NWs used for PL testing was in the range of 220-280 nm.

In the optomechanical characterization experiment, we measured the PL spectra of single InGaN/GaN NWs under different contact/compression force levels. Fig. 7(c) shows the SEM photograph of an AFM probe tip contacting the top surface of an InGaN/GaN NW. The AFM probe was employed for applying a compression force in the range of 0-5 μN along the vertical direction to the NW. The 0 μN contact force refers to a gentle contact between the AFM tip and the NW sample with a force level not measurable by the AFM beam deflection. Fig. 7(e) presents the schematics of the optomechanical testing setup and the characterization flow, and Fig. 7(f) shows the SEM photograph of the experimental implementation. The PL emission from the InGaN/GaN NW was measured by the optical testing module at room temperature. The two microfibers were firstly positioned to the proximity of a single NW and covered the entire external surface of the NW. As shown in the inset of Fig. 7(f), a single InGaN/GaN NW with diameter of 251 nm grown between two straight-slot-shape markers on Si substrate was tested for PL measurement. Two adjacent NWs have a pitch of 1 mm to avoid any optical crosstalk between them during PL testing. Laser (wavelength: 405 nm) was then used for NW excitation via the illumination fiber. Once a contact/compression force was applied to the NW top surface by the protruding AFM probe, the PL spectrum was collected through the detection fiber and measured by the coupled spectrometer.

Prior to performing the PL measurement on a particular NW, we calibrated the relationship of the applied force vs. the nanomanipulator displacement. The contact force was quantified through the measurement method described in Section II-C. The measured force-displacement curve for the NW in Fig. 7(f) is shown Fig. 7(d). Once the probe-NW contact was established, we controlled the nanomanipulator displacement to compress the NW to a desired contact/compression force level.

Fig. 7(g) presents the PL spectra of the NW in Fig. 7(f) as a function of the applied compression force. Under all the force levels, the PL spetrum peaks remained nearly constant at ∼612 nm (orange light emission; 611.819 nm at 0 N, 612.019 nm at 3 μN, 612.322 nm at 4 μN, 612.591 nm at 5 μN), and consistent full width at half maximum (FWHM) (163.951 nm for 0 N, 163.899 nm for 3 μN, 164.122 nm for 4 μN, 163.899 nm for 5 μN) could be observed. However, we observed slightly reduced PL intensities with the compression force increased. The PL spectrum peak intensity reduced by 4%, 9.25%, and 13.9% from that of the non-compressed condition at force levels of 3 μN, 4 μN, and 5 μN, respectively. This compression-induced PL peak reduction can be attributed to the increased piezoelectric polarization [43].

C. Optoelectronic Characterization

We then performed the EL testing of single InGaN/GaN NWs under different levels of injected electrical current through electrical nanoprobing. As schematically shown in Fig. 8(a), our InGaN/GaN NW samples were vertically grown on a Si substrate. Under the optimal growth condition, the NW's emission wavelength can be adjusted by tuning the NW diameter in the range of 200-600 nm [44]. Thus, each NW can serve as a single-pixel light-emitting diode (LED). The NWs have a near-perfect hexagonal morphology and smooth lateral surface, which contribute to the enhanced light emission performance from the NW top surface.

To passivate the vertical side wall of the NW and avoid short circuit risk during two-point electrical probing (due to the coating of Ni/Au electrodes on NW top surface), a polyimide resist layer was spin-coated onto the NW growth substrate

Authorized licensed use limited to: The University of Toronto. Downloaded on March 24,2022 at 15:58:40 UTC from IEEE Xplore. Restrictions apply.

This article has been accepted for inclusion in a future issue of this journal. Content is final as presented, with the exception of pagination.

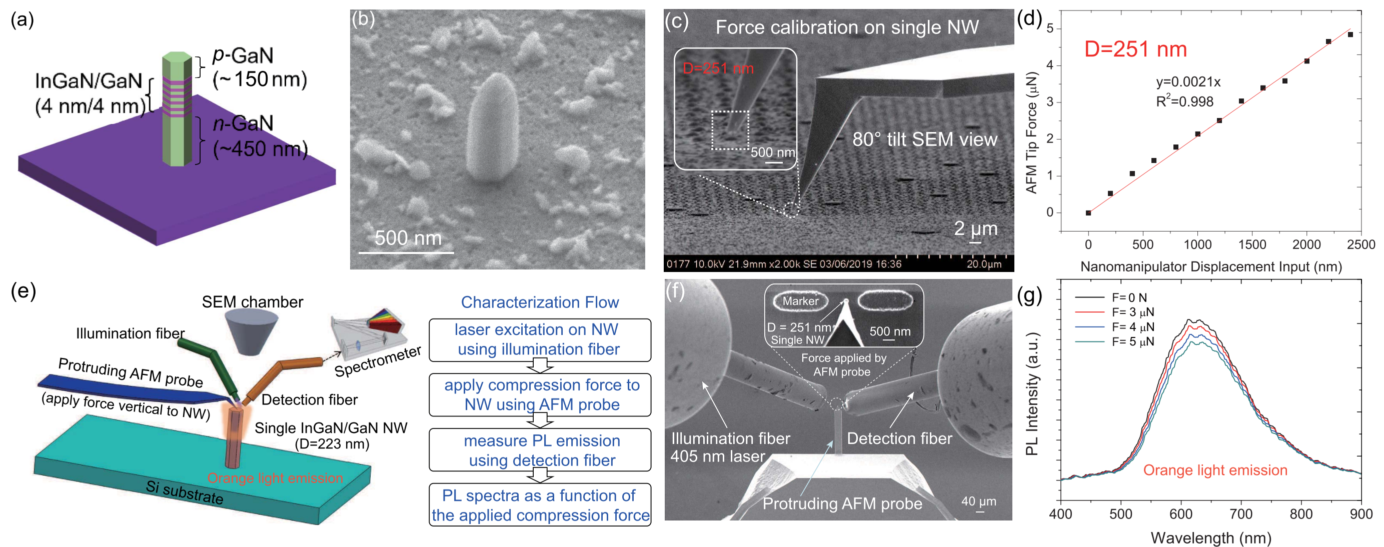

Fig. 7. Optomechanical characterization of InGaN/GaN NWs. (a) Schematic structure of the InGaN/GaN quantum-dot NW grown a Si substrate. (b) 45°-tilting SEM photograph of a single InGaN/GaN NW. (c) SEM photograph of the force-displacement calibration setup. (d) Force-displacement curve obtained from a NW of 251 nm in diameter. (e) Schematics of the optomechanical testing setup and the characterization flow. (f) SEM photograph of the implemented optomechanical testing setup. (g) PL spectra of the NW as a function of the applied contact/compression force.

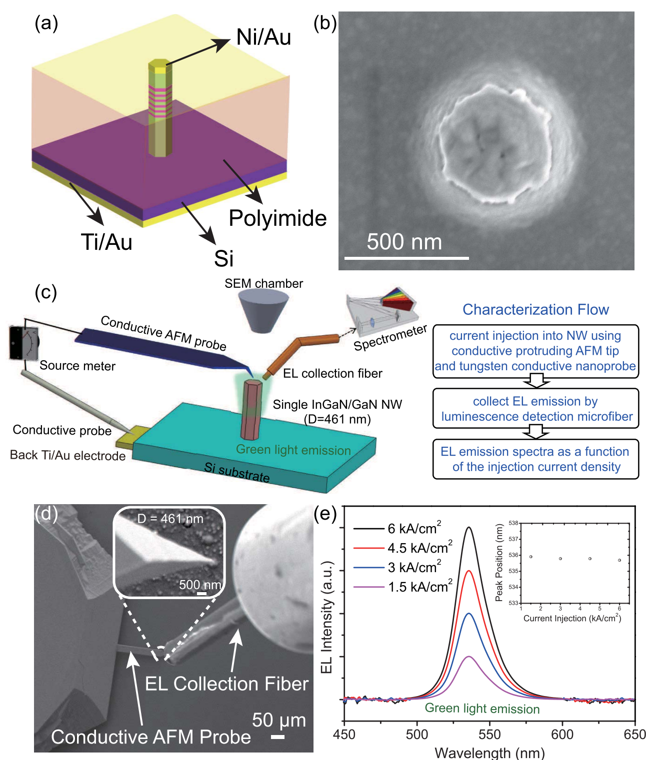

Fig. 8. Optoelectronic characterization of InGaN/GaN NWs. (a) Schematic of a single InGaN/GaN NW LED as the EL testing sample. (b) Top-view SEM image of the exposed p-GaN nanowire top-surface after polyimide passivation and dry etching. (c) Schematics of the optoelectronic testing setup and the characterization flow. (d) SEM photograph of implemented EL characterization setup. (e) EL emission spectra as a function of injection current for a single NW with diameter of 461 nm.

to fully cover the NWs and then oxygen-plasma-etched to expose the NW top surface [Fig. 8(b)]. To minimize the contact resistance between the conductive probes and the NW sample, a Ti/Au (20 nm/ 100 nm) electrode was deposited at the backside of the Si substrate and a Ni/Au (10 nm/10 nm) electrode was deposited on the NW top surface using e-beam evaporation, and then annealed at ~500 °C for 1 min in nitrogen environment. Fig. 8(b) shows the SEM photograph of a NW top surface coated with the Ni/Au electrode.

Fig. 8(c) shows the schematics of the optoelectronic testing setup and the characterization flow, and Fig. 8(d) shows the SEM photograph of the implemented EL characterization setup. The conductive protruding AFM probe and the tungsten conductive nanoprobe [not shown in Fig. 8(d)] were employed for injecting a current into a NW of 461 nm in diameter. In the meanwhile, the EL emission was collected by the luminescence detection microfiber.

Fig. 8(e) illustrates the EL emission spectrum as a function of the injection current density. The measured EL spectra exhibit a peak emission wavelength of ~536 nm (green light emission; 535.891 nm for 1.5 kA/cm^2, 535.789 nm for 3 kA/cm^2, 535.854 nm for 4.5 kA/cm^2, and 535.765 nm for 6 kA/cm^2), and the EL peak intensity increased proportionally with the injection current density. The inset of Fig. 8(e) indicates no significant shift in the EL emission peak position with the injection current density increased, suggesting a low level of quantum-confined Stark effect (QCSE). This is due to the highly efficient strain relaxation of the NW structure [44].

D. Electromechanical Characterization

In this section, we demonstrated the system's capability of electromechanical characterization of single NWs. We measured the current-voltage (I-V) characteristics of single InGaN/GaN NWs at different contact/compression force levels. Fig. 9(a) shows the SEM photograph of an AFM probe tip applying a vertical force to the top surface of an InGaN/GaN NW. Fig. 9(b) shows the force-displacement calibration curve for compressing a NW of 223 nm in diameter, which was used for applying desired contact force level to the same InGaN/GaN NW during I-V characterization.

Authorized licensed use limited to: The University of Toronto. Downloaded on March 24,2022 at 15:58:40 UTC from IEEE Xplore. Restrictions apply.

This article has been accepted for inclusion in a future issue of this journal. Content is final as presented, with the exception of pagination.

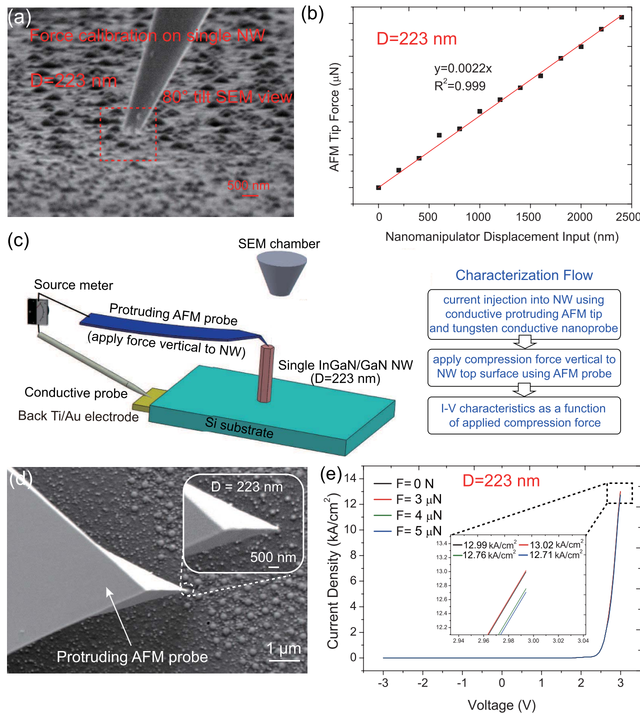

Fig. 9. Electromechanical characterization of single InGaN/GaN NWs. (a) SEM photograph of the force calibration setup. (b) Force calibration result for a NW of 223 nm in diameter. (c) Designed 3D schematic electromechanical testing setup and characterization flow. (d) SEM photograph of implemented electromechanical characterization setup. (e) Current-voltage characteristics of the NW (diameter: 223 nm) as a function of applied compression force.

Fig. 9(c) illustrates the schematics of the electromechanical testing setup and the characterization flow, and Fig. 9(d) displays the SEM photograph of the implemented electromechanical characterization setup. The conductive protruding AFM probe and the tungsten conductive nanoprobe [not shown in Fig. 9(d)] were firstly employed for injecting a current into the NW of 223 nm [see inset of Fig. 9(d)] for I-V measurement of the NW at room temperature, with a sweeping voltage from -3V to 3V, a step increment of 0.06 V, and a ramp rate of 100 V/s. For electrical probing of the NW, a contact/compression force (0-5 μN) was applied to the NW top surface by the protruding AFM probe. During the I-V measurement, the e-beam radiation from the SEM was switched off using a beam blanker to avoid any electrical noise induced by the incident electrons. In addition, before each measurement the protruding AFM probe connecting the top surface of InGaN/GaN NWs was first grounded to eliminate any charge buildup on the sample due to SEM imaging.

Fig. 9(e) presents the I-V curves of the InGaN/GaN NW (223 nm) measured under the compression force levels of 0-5 μN. The NW have a turn-on voltage of $\sim$2.5 V, which is better than previously reported values (3-3.5 V) in ensemble nanowire LEDs [45] and GaN-based planar devices [46]. In addition, consistent I-V characteristics with current densities in the range of 12.71-13.02 kA/cm^2 at 3 V (12.99 kA/cm^2 at 0 N, 13.02 kA/cm^2 at 3 μN, 12.76 kA/cm^2 at 4 μN, 12.71 kA/cm^2 at 5 μN) were observed from the same NW under different compression force levels, confirming that the InGaN/GaN NW had stable electronic properties under external mechanical compression.

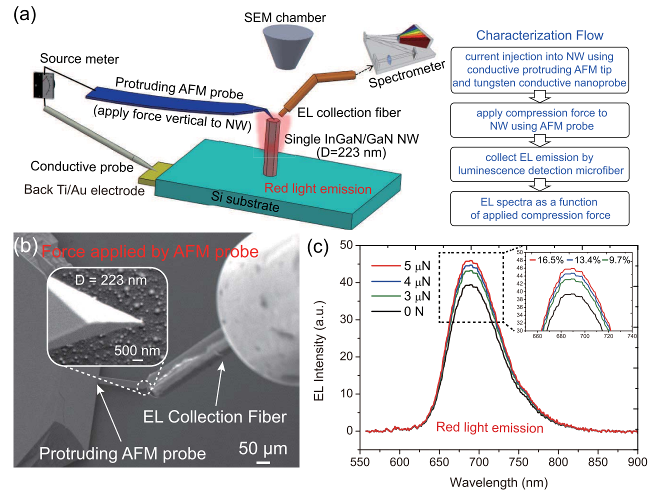

Fig. 10. Mechano-optoelectronic characterization of single InGaN/GaN NWs. (a) Designed 3D schematic mechano-optoelectronic testing setup and characterization flow. (b) SEM photograph of implemented mechano-optoelectronic setup. (c) EL emission spectra as a function of applied compression force, for a NW of 223 nm in diameter.

E. Mechano-Optoelectronic Characterization

For packaging vertically-grown InGaN/GaN NWs into an LED, a transparent indium tin oxide (ITO) electrode needs to be applied on top surfaces of the NWs to form a top-bottom electrode pair for current injection [46]. This packaging process imposes a mechanical strain/stress on the NWs, which may affect the optoelectronic properties of the NWs and thus the performance of the fabricated LEDs. To date, there is no experimental study on how the mechanical effect of the NW packaging condition affects the optoelectronic properties of the NWs. Leveraging the unique capability of our system for field-coupled testing of single NWs, we performed, for the first time, the mechano-optoelectronic characterization of single InGaN/GaN NWs.

In the mechano-optoelectronic testing experiments, we measured the EL spectra of a single InGaN/GaN NW under different contact/compression force levels. Fig. 10(a) illustrates the schematics of the mechano-optoelectronic testing setup and the characterization flow, and Fig. 10(b) displays the SEM photograph of the implemented mechano-optoelectronic characterization setup. The conductive AFM probe and the tungsten conductive nanoprobe [not shown in Fig. 10(b)] were employed for injecting a current of 4.2 μA into the NW; in the meanwhile, a compression force in the range of 0-5 μN was applied along the vertical direction to the NW by the AFM tip. Finally, the EL emission spectrum was collected using the luminescence detection microfiber [Fig. 10(a)] coupled to the high-precision spectrometer.

Fig. 10(c) shows the EL emission spectra of the InGaN/GaN NW (diameter: 223 nm) under compression forces of 0 μN, 3 μN, 4 μN, and 5 μN. At 0 μN, the measured EL spectrum exhibits a peak emission wavelength of 686 nm (red light),

Authorized licensed use limited to: The University of Toronto. Downloaded on March 24,2022 at 15:58:40 UTC from IEEE Xplore. Restrictions apply.

This article has been accepted for inclusion in a future issue of this journal. Content is final as presented, with the exception of pagination.

and the corresponding FWHM of the EL spectrum is 74 nm. Once a compression force was applied to the NW top surface, the EL spectrum peak intensity increased by 9.7% at 3 μN, 13.4% at 4 μN, and 16.5% at 5 μN. This compression-induced EL enhancement of the NW could be explained by the QCSE. The compression force was applied along the growth direction of the Ga-polar single NW, and thus induced a compression strain (0.5389%, derived from strain simulation) along the c-direction and the basal plane of the InGaN/GaN wurtzite crystal structure. Combining the compressive strain with the polarization-related constants reported in the literature [47]–[49], the reduction of piezoelectric polarization [43] of the tested NW (223 nm) was estimated to be 0.00505 C/m^2 with the 5 μN compression. The derived reduction of piezoelectric polarization has weakened the QCSE accordingly, which could explain the slight enhancement of EL peak intensity [50].

IV. Discussion

The presented field-coupled characterization experiments on single InGaN/GaN NWs have fully demonstrated the unique merits of the developed SEM-based nanomanipulation system. Firstly, in the design of SEM-based optical characterization module, we employed the space-saving optical microfibers instead of the conventional sizeable paraboloidal mirrors, which created enough space for integration of multiphysical end-effectors in the SEM vacuum chamber. Besides, in the design of SEM-based mechanical characterization module, the protruding AFM probe tip was selected instead of the standard AFM probe, which allowed the direct visualization of tip-sample contact and the dual function of the AFM probe as an mechanical and electrical end-effector. Secondly, the high positioning resolution (0.1 nm) of the developed nanomanipulation system has enabled multiple challenging manipulation and characterization tasks on single InGaN/GaN NWs, including the establishment of stable AFM probe-NW contact, the application of micronewton-level compression force on the NW top surface, and the high-efficiency collection of EL/PL luminescence. Furthermore, another major merit of the developed system is its high flexibility for conducting different field-coupled characterization tasks, which has been demonstrated in the presented characterization experiments of single InGaN/GaN NWs.

In future work, we will automate some key steps of the SEM-based multiphysical nanomaterial manipulation technique, to realize additional functionalities such as automatic electrical nanoprobing, closed-loop contact force control, and vision-based automatic alignment of the optical microfibers and the nano-sample. In addition, we also aim to apply the developed system to other types of one-dimensional (e.g., nanorods, nanotubes, and nanobelts) and two-dimensional (e.g., nano-films and mono/few-layer 2D materials) nanostructures, making it a versatile platform for multiphysical nanomaterial characterization.

V. Conclusion

This paper reported the development of the first SEM-based nanomanipulation system for multiphysical characterization of single nanomaterials. With seamless integration of multiphysical testing modules, the system is capable of executing *in-situ* field-coupled nanomaterial characterization tasks on single InGaN/GaN NWs, including optomechanical, optoelectronic, electromechanical, and mechano-optoelectronic characterization. Using the developed system, we have carried out the first investigation of the mechanical impact on the EL property of single InGaN/GaN NWs. The system will serve as a versatile platform for nanomaterial characterization, which could provide useful guidance for nanomaterial synthesis and nanodevice applications.

Acknowledgment

Some intellectual properties related to the nanowire synthesis and preparation methods have been licensed to NS Nanotech Inc., which was co-founded by Zetian Mi. The University of Michigan and Mi have a financial interest in NS Nanotech.

References

[1] S. Choi, H. Lee, R. Ghaffari, T. Hyeon, and D.-H. Kim, "Recent advances in flexible and stretchable bio-electronic devices integrated with nanomaterials," *Adv. Mater.*, vol. 28, no. 22, pp. 4203–4218, 2016.

[2] J. H. Lee, M. H. Kim, and H. R. Moon, "Nanocomposite synthesis strategies based on the transformation of well-tailored metal–organic frameworks," *Chem. Commun.*, vol. 57, no. 57, pp. 6960–6974, 2021.

[3] M. Casini, *Smart Buildings: Advanced Materials and Nanotechnology to Improve Energy-Efficiency and Environmental Performance*. Sawston, U.K.: Woodhead Publishing, 2016.

[4] P. Song, H. Fu, Y. Wang, C. Chen, P. Ou, R. T. Rashid, S. Duan, J. Song, Z. Mi, and X. Y. Liu, "A microfluidic field-effect transistor biosensor with rolled-up indium nitride microtubes," *Biosens. Bioelectron.*, vol. 190, 2021, Art. no. 113264.

[5] H. Kim *et al.*, "Multifunctional photonic nanomaterials for diagnostic, therapeutic, and theranostic applications," *Adv. Mater.*, vol. 30, no. 10, Mar. 2018, Art. no. 1701460.

[6] C. Shi *et al.*, "Recent advances in nanorobotic manipulation inside scanning electron microscopes," *Microsyst. Nanoeng.*, vol. 2, no. 1, p. 16024, Dec. 2016.

[7] J. Qu, R. Wang, Y. Sun, I. Shih, Z. Mi, and X. Liu, "Characterizing the electrical breakdown properties of single n-i-n-n$^+$: GaN nanowires," *Appl. Phys. Lett.*, vol. 113, no. 19, Nov. 2018, Art. no. 193103.

[8] C. Ru *et al.*, "Automated four-point probe measurement of nanowires inside a scanning electron microscope," *IEEE Trans. Nanotechnol.*, vol. 10, no. 4, pp. 674–681, Jul. 2011.

[9] Y. L. Zhang, Y. Zhang, C. Ru, B. K. Chen, and Y. Sun, "A load-lock-compatible nanomanipulation system for scanning electron microscope," *IEEE/ASME Trans. Mechatronics*, vol. 18, no. 1, pp. 230–237, Feb. 2013.

[10] H. Zeng, T. Li, M. Bartenwerfer, S. Fatikow, and Y. Wang, "*In situ* SEM electromechanical characterization of nanowire using an electrostatic tensile device," *J. Phys. D, Appl. Phys.*, vol. 46, no. 30, Jul. 2013, Art. no. 305501.

[11] S. Zimmermann, T. Tiemerding, and S. Fatikow, "Automated robotic manipulation of individual colloidal particles using vision-based control," *IEEE/ASME Trans. Mechatronics*, vol. 20, no. 5, pp. 2031–2038, Oct. 2015.

[12] F. Schmoeckel and S. Fatikow, "Smart flexible microrobots for scanning electron microscope (SEM) applications," *J. Intell. Mater. Syst. Struct.*, vol. 11, no. 3, pp. 191–198, Mar. 2000.

[13] S. Fatikow, T. Wich, H. Hulsen, T. Sievers, and M. Jahnisch, "Microrobot system for automatic nanohandling inside a scanning electron microscope," *IEEE/ASME Trans. Mechatronics*, vol. 12, no. 3, pp. 244–252, Jun. 2007.

[14] D. J. Bell, L. X. Dong, B. J. Nelson, M. Golling, L. Zhang, and D. Grutzmacher, "Fabrication and characterization of three-dimensional InGaAs/GaAs nanosprings," *Nano Lett.*, vol. 6, no. 4, pp. 725–729, 2006.

[15] T. Fukuda, F. Arai, and M. Nakajima, *Nanomanipulation System Under Electron Microscope*. Berlin, Germany: Springer, 2013, pp. 163–196.

Authorized licensed use limited to: The University of Toronto. Downloaded on March 24,2022 at 15:58:40 UTC from IEEE Xplore. Restrictions apply.

This article has been accepted for inclusion in a future issue of this journal. Content is final as presented, with the exception of pagination.

[16] T. Fukuda, F. Arai, and L. Dong, "Assembly of nanodevices with carbon nanotubes through nanorobotic manipulations," *Proc. IEEE*, vol. 91, no. 11, pp. 1803–1818, Nov. 2003.

[17] H. Ding *et al.*, "Visual servoing-based nanorobotic system for automated electrical characterization of nanotubes inside SEM," *Sensors*, vol. 18, no. 4, p. 1137, Apr. 2018.

[18] G. Li, N. Xi, H. Chen, A. Saeed, and M. Yu, "Assembly of nanostructure using AFM based nanomanipulation system," in *Proc. IEEE Int. Conf. Robot. Autom. (ICRA)*, vol. 1, Apr./May 2004, pp. 428–433.

[19] G. Li, N. Xi, M. Yu, and W.-K. Fung, "Development of augmented reality system for AFM-based nanomanipulation," *IEEE/ASME Trans. Mechatronics*, vol. 9, no. 2, pp. 358–365, Jun. 2004.

[20] G. Li, N. Xi, H. Chen, C. Pomeroy, and M. Prokos, "'Videolized' atomic force microscopy for interactive nanomanipulation and nanoassembly," *IEEE Trans. Nanotechnol.*, vol. 4, no. 5, pp. 605–615, Sep. 2005.

[21] H. Xie, D. S. Haliyo, and S. Régnier, "A versatile atomic force microscope for three-dimensional nanomanipulation and nanoassembly," *Nanotechnology*, vol. 20, no. 21, May 2009, Art. no. 215301.

[22] S. Yuan, Z. Wang, N. Xi, Y. Wang, and L. Liu, "AFM tip position control *in situ* for effective nanomanipulation," *IEEE/ASME Trans. Mechatronics*, vol. 23, no. 6, pp. 2825–2836, Dec. 2018.

[23] J. Hou *et al.*, "AFM-based robotic nano-hand for stable manipulation at nanoscale," *IEEE Trans. Autom. Sci. Eng.*, vol. 10, no. 2, pp. 285–295, Apr. 2013.

[24] L. Liu, Y. Luo, N. Xi, Y. Wang, J. Zhang, and G. Y. Li, "Sensor referenced real-time videolization of atomic force microscopy for nanomanipulations," *IEEE/ASME Trans. Mechatronics*, vol. 13, no. 1, pp. 76–85, Feb. 2008.

[25] X. Wei, Q. Chen, L. Peng, R. Cui, and Y. Li, "*In situ* measurements on individual thin carbon nanotubes using nanomanipulators inside a scanning electron microscope," *Ultramicroscopy*, vol. 110, no. 3, pp. 182–189, Feb. 2010.

[26] L. J. Brillson, "Nanoscale luminescence spectroscopy of defects at buried interfaces and ultrathin films," *J. Vacuum Sci. Technol. B, Microelectron. Nanometer Struct. Process., Meas., Phenomena*, vol. 19, no. 5, pp. 1762–1768, 2001.

[27] J. H. Choi *et al.*, "GaN light-emitting diodes on glass substrates with enhanced electroluminescence," *J. Mater. Chem.*, vol. 22, no. 43, pp. 22942–22948, 2012.

[28] J. B. Baxter, F. Wu, and E. S. Aydil, "Growth mechanism and characterization of zinc oxide hexagonal columns," *Appl. Phys. Lett.*, vol. 83, no. 18, pp. 3797–3799, Nov. 2003.

[29] C. Li *et al.*, "*In situ* comprehensive characterization of optoelectronic nanomaterials for device purposes," *Nanotechnology*, vol. 20, no. 17, Apr. 2009, Art. no. 175703.

[30] J. H. He, P. H. Chang, C. Y. Chen, and K. T. Tsai, "Electrical and optoelectronic characterization of a ZnO nanowire contacted by focused-ion-beam-deposited Pt," *Nanotechnology*, vol. 20, no. 13, Apr. 2009, Art. no. 135701.

[31] B. G. Yacobi and D. B. Holt, "Cathodoluminescence scanning electron microscopy of semiconductors," *J. Appl. Phys.*, vol. 59, no. 4, pp. R1–R24, Feb. 1986.

[32] J. Qu *et al.*, "An SEM-based nanomanipulation system for multi-physical characterization of single InGaN/GaN nanowires," in *Proc. IEEE/RSJ Int. Conf. Intell. Robots Syst. (IROS)*, Oct. 2020, pp. 2866–2871.

[33] A. Vilà *et al.*, "Fabrication of metallic contacts to nanometre-sized materials using a focused ion beam (FIB)," *Mater. Sci. Eng. C*, vol. 26, nos. 5–7, pp. 1063–1066, Jul. 2006.

[34] G. D. Marzi, D. Iacopino, A. J. Quinn, and G. Redmond, "Probing intrinsic transport properties of single metal nanowires: Direct-write contact formation using a focused ion beam," *J. Appl. Phys.*, vol. 96, no. 6, pp. 3458–3462, Sep. 2004.

[35] R. S. Gates, "Experimental confirmation of the atomic force microscope cantilever stiffness tilt correction," *Rev. Sci. Instrum.*, vol. 88, no. 12, Dec. 2017, Art. no. 123710.

[36] S. Belikov, J. Alexander, C. Wall, I. Yermolenko, S. Magonov, and I. Malovichko, "Thermal tune method for AFM oscillatory resonant imaging in air and liquid," in *Proc. Amer. Control Conf.*, Jun. 2014, pp. 1009–1014.

[37] S. A. Edwards, W. A. Ducker, and J. E. Sader, "Influence of atomic force microscope cantilever tilt and induced torque on force measurements," *J. Appl. Phys.*, vol. 103, no. 6, Mar. 2008, Art. no. 064513.

[38] J. Qu, M. Lee, M. Hilke, and X. Liu, "Investigating the impact of SEM chamber conditions and imaging parameters on contact resistance of *in situ* nanoprobing," *Nanotechnology*, vol. 28, no. 34, 2017, Art. no. 345702.

[39] Y.-H. Ra, R. Navamathavan, H.-I. Yoo, and C.-R. Lee, "Single nanowire light-emitting diodes using uniaxial and coaxial InGaN/GaN multiple quantum wells synthesized by metalorganic chemical vapor deposition," *Nano Lett.*, vol. 14, no. 3, pp. 1537–1545, Feb. 2014.

[40] A. D. L. Bugallo *et al.*, "Single-wire photodetectors based on InGaN/GaN radial quantum wells in GaN wires grown by catalyst-free metal-organic vapor phase epitaxy," *Appl. Phys. Lett.*, vol. 98, no. 23, Jun. 2011, Art. no. 233107.

[41] K. Kishino, H. Sekiguchi, and A. Kikuchi, "Improved Ti-mask selective-area growth (SAG) by RF-plasma-assisted molecular beam epitaxy demonstrating extremely uniform GaN nanocolumn arrays," *J. Cryst. Growth*, vol. 311, no. 7, pp. 2063–2068, 2009.

[42] A. Bengoechea-Encabo *et al.*, "Understanding the selective area growth of GaN nanocolumns by MBE using Ti nanomasks," *J. Cryst. Growth*, vol. 325, no. 1, pp. 89–92, Jun. 2011.

[43] W.-C. Tsai *et al.*, "Suppressed piezoelectric polarization in single InGaN/GaN heterostructure nanowires," *Phys. Rev. B, Condens. Matter*, vol. 88, no. 15, Oct. 2013, Art. no. 155323.

[44] Y.-H. Ra *et al.*, "Full-color single nanowire pixels for projection displays," *Nano Lett.*, vol. 16, no. 7, pp. 4608–4615, Jul. 2016.

[45] Z. Gong *et al.*, "Size-dependent light output, spectral shift, and self-heating of 400 nm InGaN light-emitting diodes," *J. Appl. Phys.*, vol. 107, no. 1, 2010, Art. no. 013103.

[46] R. Wang, X. Liu, I. Shih, and Z. Mi, "High efficiency, full-color AlInGaN quaternary nanowire light emitting diodes with spontaneous core-shell structures on Si," *Appl. Phys. Lett.*, vol. 106, no. 26, 2015, Art. no. 261104.

[47] A. Polian, M. Grimsditch, and I. Grzegory, "Elastic constants of gallium nitride," *J. Appl. Phys.*, vol. 79, no. 6, pp. 3343–3344, 1996.

[48] H. Qin, X. Luan, C. Feng, D. Yang, and G. Zhang, "Mechanical, thermodynamic and electronic properties of wurtzite and zinc-blende GaN crystals," *Materials*, vol. 10, no. 12, p. 1419, Dec. 2017.

[49] F. Bernardini, V. Fiorentini, and D. Vanderbilt, "Accurate calculation of polarization-related quantities in semiconductors," *Phys. Rev. B, Condens. Matter*, vol. 63, no. 19, Apr. 2001, Art. no. 193201.

[50] N. Nanhui *et al.*, "Enhanced luminescence of InGaN/GaN multiple quantum wells by strain reduction," *Solid-State Electron.*, vol. 51, no. 6, pp. 860–864, Jun. 2007.

Juntian Qu (Member, IEEE) received the B.Eng. and M.Eng. degrees in automatic control theory and engineering from Northeastern University, Shenyang, China, in 2012 and 2014, respectively, and the Ph.D. degree in mechanical engineering from McGill University, Montreal, QC, Canada, in 2019.

He is currently the Shuimu Post-Doctoral Fellow and an Assistant Research Fellow with the Department of Mechanical Engineering, Tsinghua University, and the Incoming Assistant Professor with the Tsinghua Shenzhen International Graduate School, Tsinghua University. His current research interests include SEM-based robotic micro and nano manipulation, nanomaterial characterization, MEMS, and 3D printing.

Renjie Wang received the B.Sc. degree in engineering from Zhejiang University in 2010, the M.Sc. degree in mechanical engineering from the University of Houston in 2013, and the Ph.D. degree in electrical engineering from McGill University in 2018.

Currently, he is working on design, simulation, fabrication, and characterizations of on-chip waveguide optical amplifiers and lasers as a Post-Doctoral Researcher of Engineering Physics at McMaster University. His expertise include III-nitride, Si, and Ge semiconductor and their optoelectronic device applications, heteroepitaxy, nano-scale and micro-scale fabrication, and materials/optoelectronic characterizations.

Authorized licensed use limited to: The University of Toronto. Downloaded on March 24,2022 at 15:58:40 UTC from IEEE Xplore. Restrictions apply.

This article has been accepted for inclusion in a future issue of this journal. Content is final as presented, with the exception of pagination.

Peng Pan (Member, IEEE) received the B.Eng. and M.Eng. degrees in mechanical engineering from Soochow University, Suzhou, China, in 2013 and 2016, respectively, and the Ph.D. degree in mechanical engineering from McGill University, Montreal, QC, Canada, in 2021.

Currently, he is a Post-Doctoral Researcher with the Department of Mechanical and Industrial Engineering, University of Toronto, Toronto, ON, Canada. His research interests include automated robotic manipulation, microelectromechanical systems (MEMS), microfluidics, and large-scale gene screening. His research interests include automated robotic manipulation, MEMS, and microfluidics.

Linghao Du received the B.E. degree in mechanical engineering from the South China University of Technology, Guangzhou, China, in 2018, and the M.A.Sc. degree in mechanical engineering from the University of Toronto, ON, Canada, in 2020.

He was affiliated with the Department of Mechanical and Industrial Engineering and the Robotics Institute, University of Toronto, at the time of the work and is currently affiliated with the Human-Machine Interaction Laboratory, Huawei, Canada. His research interests include human–computer interaction, robotics, and 3D computer vision.

Zetian Mi (Fellow, IEEE) received the Ph.D. degree in applied physics from the University of Michigan, Ann Arbor, in 2006.

He was a Faculty Member at McGill University from 2007 to 2016. He is a Professor with the Department of Electrical Engineering and Computer Science, University of Michigan. He is a Co-Founder of NS Nanotech Inc. and NX Fuels Inc. His teaching and research interests are in the areas of low dimensional semiconductors and their applications in photonic, electronic, clean energy, and quantum devices and systems. He is a fellow of OSA and SPIE. While working with McGill University, he received several awards, including the Hydro-Québec Nano-Engineering Scholar Award in 2009, the William Dawson Scholar Award in 2011, the Christophe Pierre Award for Research Excellence in 2012, and the Engineering Innovation Award in 2015. He has received the Science and Engineering Award from W. M. Keck Foundation in 2020 and the David E. Liddle Research Excellence Award in 2021. He has also received the Young Investigator Award from the 27th North American Molecular Beam Epitaxy (MBE) Conference in 2010, the Young Scientist Award from the International Symposium on Compound Semiconductors in 2015, and the IEEE Photonics Society Distinguished Lecturer Award in 2020. He has served as the chair for many international conferences, including the General Chair for IEEE Photonics Society Summer Topicals Meeting from 2016 to 2017, the Program Chair for 30th North American Conference in 2013, the Co-Chair for International Symposium on Semiconductor Light Emitting Devices in 2017, the General Chair for IEEE Photonics Conference in 2020, and the Program Chair for Compound Semiconductor Week in 2022. He currently serves as the Editor-in-Chief for *Progress in Quantum Electronics*, a Serial Editor for *Semiconductors and Semimetals*, and the Vice President of IEEE Photonics Society's conferences.

Yu Sun (Fellow, IEEE) received the B.S. degree in electrical engineering from the Dalian University of Technology, Dalian, China, in 1996, the master's degree from the Institute of Automation, Chinese Academy of Sciences, Beijing, China, in 1999, and the Ph.D. degree in mechanical engineering from the University of Minnesota, Minneapolis, USA, in 2003.

He is a Professor and the Director of the Robotics Institute, University of Toronto. His laboratory specializes in developing innovative technologies and instruments for manipulating and characterizing cells, molecules, and nanomaterials. He was an elected fellow of American Society of Mechanical Engineers (ASME), American Association for the Advancement of Science (AAAS), National Academy of Inventors (NAI), Canadian Academy of Engineering (CAE), and Royal Society of Canada (RSC) for his work on micro-nano devices and robotic systems.

Xinyu Liu (Member, IEEE) received the B.Eng. and M.Eng. degrees from the Harbin Institute of Technology, Harbin, China, in 2002 and 2004, respectively, and the Ph.D. degree from the University of Toronto, Toronto, ON, Canada, in 2009, all in mechanical engineering.

He is currently the Percy Edward Hart Professor with the Department of Mechanical and Industrial Engineering and cross-appointed with the Institute of Biomedical Engineering, University of Toronto. Before joining the University of Toronto in September 2017, he was an Associate Professor and the Canada Research Chair of Microfluidics and BioMEMS with the Department of Mechanical Engineering, McGill University, Montreal, QC, Canada. His research interests include microrobotics, nanorobotics, and soft robotics, microfluidics, and BioMEMS.

Dr. Liu was a recipient of the Stars in Global Health Award from Grand Challenges Canada in 2012, the Douglas R. Colton Medal for Research Excellence from CMC Microsystems in 2013, the Christophe Pierre Award for Research Excellence from McGill University in 2017, the Young Scientist Award from the Microsystems and Nanoengineering Summit in 2018, and the Highly Cited Paper Award from *Microsystems and Nanoengineering* in 2020. He is a Senior Editor of the IEEE ROBOTICS AND AUTOMATION LETTERS, an Editor of *Microsystems and Nanoengineering*, and an Associate Editor of the IEEE TRANSACTIONS ON AUTOMATION SCIENCE AND ENGINEERING, the IEEE TRANSACTIONS ON NANOTECHNOLOGY, the *International Journal of Advanced Robotic Systems*, and the *IET Cyber-Systems and Robotics*.

Authorized licensed use limited to: The University of Toronto. Downloaded on March 24,2022 at 15:58:40 UTC from IEEE Xplore. Restrictions apply.